

1 **How do gravity waves triggered by a typhoon propagate from the**
2 **troposphere to the upper atmosphere?**

3 Qinzeng Li¹, Jiyao Xu^{1,2}, Hanli Liu³, Xiao Liu⁴, Wei Yuan¹

4 ¹State Key Laboratory of Space Weather, National Space Science Center, Chinese Academy of
5 Sciences, Beijing, 100190, China,

6 ²School of Astronomy and Space Science, University of Chinese Academy of Science, Beijing,
7 100049, China,

8 ³High Altitude Observatory, National Center for Atmospheric Research, Boulder, CO
9 80307-3000, USA,

10 ⁴School of Mathematics and Information Science, Henan Normal University, Xinxiang, 453007,
11 China,

12

13 Correspondence to: xujy@nssc.ac.cn

14 **Abstract**

15 Gravity waves (GWs) strongly affect atmospheric dynamics and photochemistry and
16 the coupling between the troposphere, stratosphere, mesosphere, and thermosphere. In
17 addition, GWs generated by strong disturbances in the troposphere (e.g., thunderstorms and
18 typhoons) can affect the atmosphere of the Earth from the troposphere to the thermosphere.
19 However, the fundamental process of GW propagation from the troposphere to the
20 thermosphere is poorly understood because it is challenging to constrain this process using
21 observations. Moreover, GWs tend to dissipate rapidly in the thermosphere because the
22 molecular diffusion increases exponentially. In this study, a double-layer airglow network
23 was used to capture concentric GWs (CGWs) over China that were excited by the Super
24 Typhoon Chaba (2016). We used ERA-5 reanalysis data and Multi-functional Transport
25 Satellite-1R observations to quantitatively describe the physical mechanism of
26 typhoon-generated CGWs propagating throughout the stratosphere, mesosphere, and
27 thermosphere. We found that the CGWs in the mesopause region were generated directly by
28 the typhoon in the troposphere. However, like the relay, the backward ray tracing analysis
29 suggested that CGWs in the thermosphere originated from the secondary waves generated
30 by the dissipation of the CGW and/or nonlinear processes in the mesopause region.

31 **1. Introduction**

32 Gravity waves (GWs) can transfer momentum and energy from the lower to upper
33 atmospheres, thereby affecting global circulation and thermal structures and the distribution
34 of chemical composition in the middle and upper atmospheres (Holton, 1983; Fritts and
35 Alexander, 2003). Studies on dynamic, photochemical, and electrodynamics processes have
36 indicated that GWs are fundamental for the coupling process between the troposphere,
37 stratosphere, mesosphere, and thermosphere (Liu and Vadas, 2013; Smith et al., 2013; Vadas
38 and Liu, 2013; Xu et al., 2015; Vadas and Becker, 2019).

39 Concentric GWs (CGWs) are a unique type of GW considered to be mainly generated
40 by convective activity in the troposphere. CGWs can also be generated by primary wave
41 breaking (Vadas and Becker, 2019; Lund et al., 2020; Kogure et al., 2020) volcanoes
42 (Duncombe, 2022), nuclear explosions (Pfeffer and Zarichny, 1962; Pierce et al., 1971), and
43 rockets (Liu et al., 2020). CGWs in the stratosphere and mesosphere generated by
44 thunderstorms have been widely reported since their sources are ubiquitous (Taylor and
45 Hapgood, 1988; Sentman et al., 2003; Suzuki et al., 2007; Yue et al., 2009; Vadas et al., 2012;
46 Xu et al., 2015; Heale et al., 2019; Smith et al., 2020). In previous studies, CGWs induced by
47 typhoons were detected using ground-based optical remote sensing (Suzuki et al., 2013)
48 while those induced by hurricanes and tropical cyclones were detected using the Suomi
49 National Polar-orbiting Partnership satellite (Yue et al., 2014; Xu et al., 2019) in the
50 mesopause region.

51 Notably, GWs tend to dissipate rapidly in the upper atmosphere due to molecular
52 viscosity and thermal diffusion (Vadas, 2007). Thermosphere GWs that are not dissipated

53 can originate directly from the troposphere (Vadas, 2007; Azeem et al., 2015) or from
54 secondary GWs, which are generated from the breaking of primary GWs in the mesosphere
55 or thermosphere region (Vadas and Fritts, 2003; Vadas and Crowley, 2010; Vadas and Azeem,
56 2021). Furthermore, Vadas and Becker (2019) for the first time presented global simulations
57 of tertiary CGWs from the dissipation of secondary CGWs in the thermosphere. Moreover,
58 wave-wave, wave-mean flow, self-acceleration, and nonlinear breaking are other potential
59 secondary wave generation mechanisms (Lund and Fritts, 2012; Fritts et al., 2015; Dong et
60 al., 2020; Fritts et al., 2020; Franke and Robinson, 1999; Zhou et al. 2002; Heale et al. 2020).
61 At the same time, tunneling has been deemed as a mechanism that can couple waves from
62 tropospheric sources to the thermosphere (Walterscheid and Hecht, 2003; Gavrilov and
63 Kshevetskii; 2018, Heale et al., 2021). However, the lack of observations of the entire
64 atmosphere limits our understanding of the fundamental process of how GWs propagate from
65 the lower atmosphere to the upper atmosphere step by step on the aspect of observations.

66 This paper presents a case study examining CGWs excited by Super Typhoon Chaba
67 (2016). To this end, we utilized Multi-functional Transport Satellite-1R (MTSAT-1R)
68 observations, multi-layer European Centre for Medium-range Weather Forecasts (ECMWF)
69 ERA-5 reanalysis data (Hoffmann et al., 2019; Hersbach et al., 2020), and high
70 spatio-temporal resolution double-layer airglow network (DLAN) (Xu et al., 2021)
71 observations. The CGW observations from the troposphere to the stratosphere and then to
72 the mesosphere were taken from MTSAT-1R, ERA-5, and the DLAN. However, given the
73 observational limitations, the DLAN was utilized to identify the mesosphere and
74 thermosphere via the ray-tracing theory. The objectives of this study were to (a) scrutinize

75 multi-layer CGW features produced by Super Typhoon Chaba (2016) from near the ground to
76 a height of 250 km, (b) to examine the entire propagation process of the CGWs excited by
77 typhoon from the lower atmosphere to the upper atmosphere, and (c) to provide new insights
78 into the coupling between different atmospheric layers.

79 **2. Data and Methods**

80 **2.1 Double layer all-sky airglow imager network data**

81 A DLAN, including an OH layer (~87 km) and OI 630.0 nm layer (~250 km) was
82 established over mainland China. The research aim of the DLAN is to explore the physical
83 mechanism of vertical and horizontal propagation and the evolution of atmospheric waves
84 triggered by severe disasters, such as typhoons, earthquakes, and tsunamis, in various middle
85 and upper atmospheric layers. The OH airglow network comprises 15 stations, including the
86 first no-gap OH airglow all-sky imager network located in northern China (Xu et al., 2015).
87 The OI 630.0 nm airglow network contains 12 stations. Each imager consists of a 1024×1024
88 pixel back-illuminated CCD detector and a Nikon 16 mm/2.8D fish-eye lens with a 180 ° field
89 of view (FOV). The OI 630.0 nm imager is operated at the 3.0 nm bandwidth filter with a
90 central wavelength of 630.0 nm. Observations using airglow optical remote sensing require
91 only a few airglow imagers to cover a wide area although it is limited by meteorological
92 conditions. Moreover, airglow observations can be used to monitor multi-layer GW activities.
93 Figure 1a and 1b illustrate the OH and OI 630.0 nm network station distribution maps,
94 respectively, in China. The OI 630.0 nm network covers nearly the entire mainland China.
95 Furthermore, the DLAN provides an excellent solution for studying the coupling process
96 among different atmospheric layers, especially the mesosphere and thermosphere.

Several standard procedures were applied to raw airglow images, including star contamination subtraction, flat fielding to remove van Rhijin, and atmospheric extinction (Li et al., 2011). The GW structure was retrieved by taking the deviation of each processed image from a half-hour running average window image. Finally, the images were projected onto the Earth's surface using the standard star map software and the altitude of the airglow layer (Garcia et al., 1997). The altitudes of the OH and OI 630.0 nm emission layers were set as approximately 87 km and 250 km, respectively.

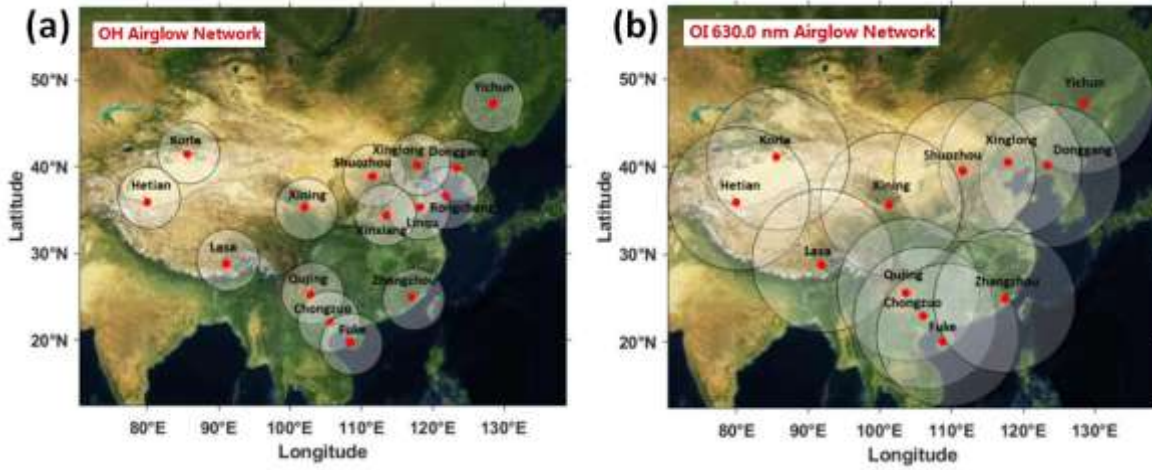
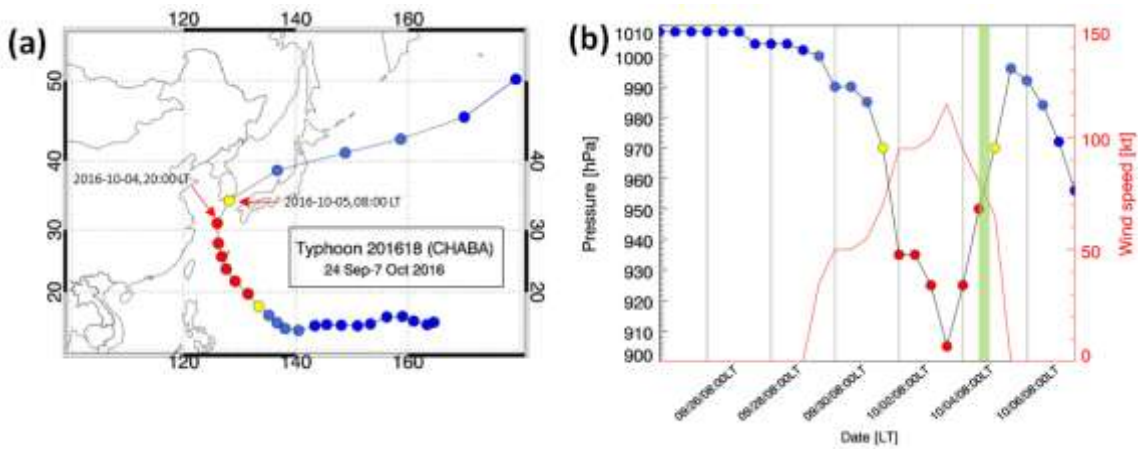


Figure 1. (a) OH airglow all-sky imager network (15 stations). **(b)** Red line (630 nm) airglow all-sky imager network (12 stations). The circles on the maps give the effective observation ranges of OH and Red line airglow imagers with diameters of about 800 km and 1800 km, respectively.

2.2 Development of Super Typhoon Chaba

Super Typhoon Chaba (2016) developed in the north-western Pacific on 24 September 2016 and its track is shown in Fig. 2a. Initially, it moved westward and then turned north-westward on 30 September. The central pressure in the eye of the typhoon and the maximum wind speed are shown in Fig. 2b. On 3 October 2016 at 20:00 LT, the typhoon was in the mature stage with a minimum central pressure of 905 hPa and maximum sustained winds of approximately 59 m/s. The typhoon moved northward on 4 October 2016 at 02:00

115 LT until 5 October 2016 at 02:00 LT. The typhoon continued moving towards the northeast
 116 and disappeared on 8 October 2016 at 02:00 LT. Consecutive satellite images of the typhoon
 117 from MTSAT-1R from 18:00 LT on 3 October 2016 to 00:00 LT on 5 October 2016 are shown
 118 in Fig. 3. MTSAT-1R, which belongs to the Japan Meteorological Agency, comprises a series
 119 of Geo-stationary Meteorological Satellites. MTSAT-1R is located at around 140 °E and
 120 covers East-Asia and the western Pacific region. The MTSAT-1R consists of four infrared
 121 channels (IR1, IR2, IR3, and IR4) and one visible channel (VIS). The MTSAT- IR1 was used
 122 in this study. The track of the typhoon was beyond the effective FOV of the OH network and
 123 at the edge of the effective FOV of the OI 630.0 nm network, which provides an excellent
 124 example for observing the CGWs stimulated by the typhoon and studying the coupling among
 125 the atmospheric layers.



126
 127 **Figure 2.** (a) The track of Typhoon Chaba is denoted by dots from 24 September to 7 October 2016 every
 128 12 hours. (b) Central pressure of Typhoon Chaba corresponding to the tracks in (a). The red line denotes
 129 the maximum sustained wind speed. The green shadow band denotes the time of ground-based airglow
 130 observation from 20:00 LT to 04:00 LT during the night of 4-5 October 2016.

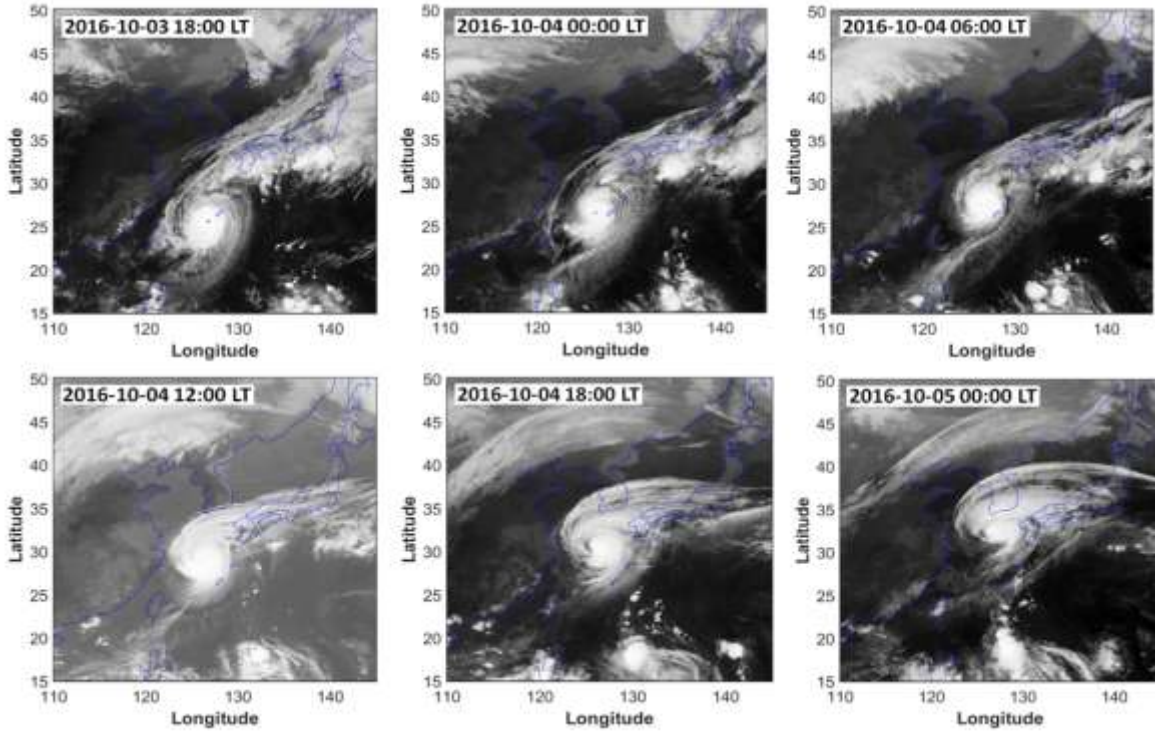


Figure 3. Consecutive satellite images of the typhoon Chaba from MTSAT-1R. The period is from 18:00 LT on 3 October 2016 to 00:00 LT on 5 October 2016, with an interval of 6 hours.

2.3 ERA-5 reanalysis data

ERA-5 is a fifth-generation ECMWF atmospheric reanalysis that provides hourly data for many atmospheric and wave parameters. ERA-5 is produced using a four-dimensional variational data assimilation algorithm based on Integrated Forecast System (IFS), with hybrid sigma/pressure (model) levels in the vertical from 1000 to 0.01 hPa (0 to 80 km). More details of the model, data assimilation system, and observation data used to produce ERA-5 were described by Hersbach et al. (2020). Horizontal reanalysis temperature and wind data with a pre-interpolated resolution of $0.25^\circ \times 0.25^\circ$ were used in this study.

2.4 Ray tracing model

We used a ray-tracing method to estimate the source location of the thermospheric secondary CGWs. The model was based on a dispersion relation that considers molecular

viscosity and thermal diffusivity (Vadas, 2007), as shown in Equation (1):

$$m^2 = \frac{k_H^2 N^2}{\omega_{lr}^2 (1 + \delta_+ + \delta^2 / \text{Pr})} \left[1 + \frac{\nu^2}{4\omega_{lr}^2} \left(k^2 - \frac{1}{4H^2} \right)^2 \frac{(1 - \text{Pr}^{-1})^2}{(1 + \delta_+ / 2)^2} \right]^{-1} - k_H^2 - \frac{1}{4H^2}, \quad (1)$$

where ω_{lr} is the intrinsic frequency; $\mathbf{k}^2 = k_H^2 + m^2$, $k_H^2 = k^2 + l^2$; H is the scale height; $\nu = \mu / \bar{\rho}$ is the kinematic viscosity where μ is the molecular viscosity and $\bar{\rho}$ is the background density; $\delta = \nu m / H \omega_{lr}$, $\delta_+ = \delta(1 + \text{Pr}^{-1})$, where Pr is the Prandtl number. k , l , and m are the zonal, meridional, and vertical wave number components of the GW, respectively. The horizontal wavelength (k_H) of the CGW was obtained from the ground-based airglow observations; $N^2 = (g/T)(dT/dz + g/c_p)$ is the square of the Brunt-Väisälä frequency, where g is the gravitational acceleration, T is the background temperature, c_p is the specific heat at constant pressure. The background temperature T and density $\bar{\rho}$ were obtained from the NRLMSISE-00 model (Picone et al., 2002).

The group velocity of the wave packet is formalized by Equation (2):

$$c_{gi} = dx_i / dt = \partial \omega / \partial k_i + V_i, \quad (2)$$

where $V_i(u, v, w)$ is the background wind, which was obtained from the Horizontal Wind Model 14 (Drob et al., 2015) and w is the vertical wind velocity, which was neglected. Using Equations (1)-(2), we yield the ground-based (zonal, meridional, and vertical) group velocity equation as follows (Vadas and Fritts, 2005):

$$c_{gx} = \frac{k}{\omega_{lr} B} \left[\frac{N^2(m^2 + 1/4H^2)}{(k^2 + 1/4H^2)^2} - \frac{\nu^2}{2} (1 - \text{Pr}^{-1})^2 \left(k^2 - \frac{1}{4H^2} \right) \frac{(1 + \delta_+ + \delta^2 / \text{Pr})}{(1 + \delta_+ / 2)^2} \right] + u, \quad (3)$$

$$c_{gy} = \frac{l}{\omega_{lr} B} \left[\frac{N^2(m^2 + 1/4H^2)}{(k^2 + 1/4H^2)^2} - \frac{\nu^2}{2} (1 - \text{Pr}^{-1})^2 \left(k^2 - \frac{1}{4H^2} \right) \frac{(1 + \delta_+ + \delta^2 / \text{Pr})}{(1 + \delta_+ / 2)^2} \right] + v, \quad (4)$$

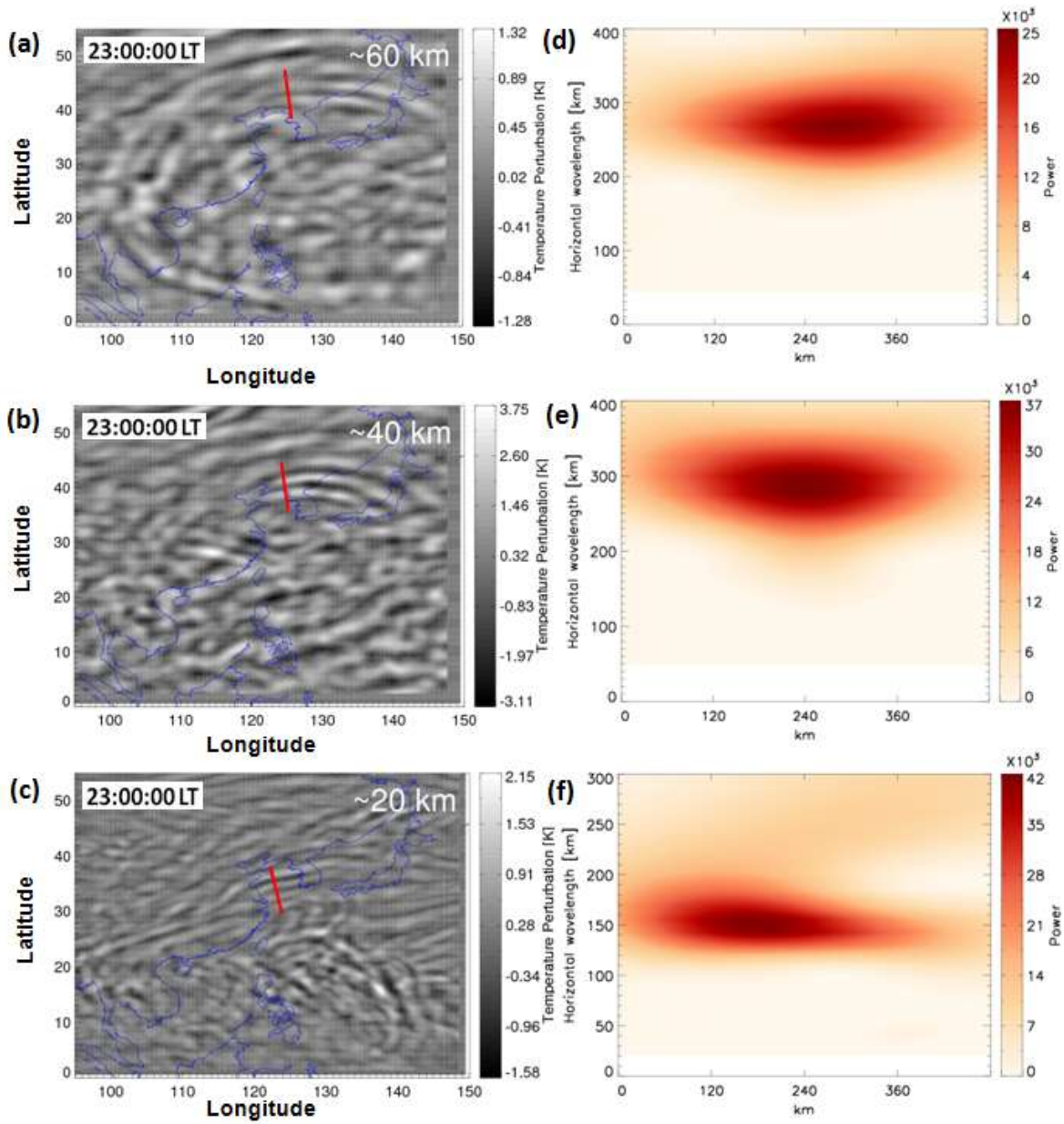
$$\begin{aligned}
c_{gz} &= \frac{1}{\omega_{lr} B} \left\{ m \left[-\frac{k_H^2 N^2}{(k^2 + 1/4H^2)^2} - \frac{\nu^2}{2} (1 - \text{Pr}^{-1})^2 \left(k^2 - \frac{1}{4H^2} \right) \frac{(1 + \delta_+ + \delta^2/\text{Pr})}{(1 + \delta_+/2)^2} \right. \right. \\
&\quad \left. \left. + \frac{\nu^4 (1 - \text{Pr}^{-1})^4}{16H^2 \omega_{lr}^2} \frac{(k^2 - 1/4H^2)^2}{(1 + \delta_+/2)^3} - \frac{\nu^2}{\text{Pr} H^2} \right] - \frac{\nu_+ \omega_{lr}}{2H} \right\}, \quad (5) \\
\text{where } B &= \left[1 + \frac{\delta_+}{2} + \frac{\delta^2 \nu^2}{16\omega_{lr}^2} (1 - \text{Pr}^{-1})^4 \frac{(k^2 - 1/4H^2)^2}{(1 + \delta_+/2)^3} \right], \nu_+ = \nu(1 + \text{Pr}^{-1}).
\end{aligned}$$

3. Results

3.1 Propagation of typhoon-induced CGWs in the stratosphere

We extracted the CGWs excited by Typhoon in the stratosphere from the ERA-5 reanalysis data. Figure 4a, 4b, and 4c show the multilayer temperature perturbations at approximately 60 km, 40 km, and 20 km at 23:00 LT, retrieved from the ERA-5 reanalysis on 4 October 2016, respectively. Temperature perturbations were calculated by subtracting the background with a 7×7 grid point running mean at 20 km and 17×17 grid point running mean at 40 km and 60 km. We found that the temperature disturbance was about ± 1.5 -2 K at 20 km and ± 3 -4 K at 40 km. Using the ECMWF reanalysis data, Kim et al. (2009) reported a similar temperature disturbance (± 4 K) at 40 km altitude. Becker et al. (2022) showed that typical temperature perturbation amplitudes simulated by a High Altitude Mechanistic general Circulation Model were ± 1 -2 K in the wintertime lower stratosphere and ± 5 K in the stratopause region. However, the temperature disturbance at 60 km altitude was only ± 1.3 K and did not increase with increasing altitude, which may be caused by this altitude being well within the sponge layer of the reanalysis model. Figure 4d, 4e, and 4f show the corresponding wavelet analysis contours of the red line in Fig. 4a, 4b, and 4c. The expansion area of CGW at the height of 20 km (Fig. 4c) was small, and the horizontal

183 wavelength was approximately 150 km from Fig. 4f. Liu et al. (2014) utilized the Whole
184 Atmosphere Community Climate model and showed that the horizontal area of the CGW
185 expansion increases with increasing altitude. The CGWs were present over a large area of
186 0°N -50°N and 100°E -150°E at approximately 60 km. The distance of the CGWs, extending
187 from the center of the circle ranged from 500 km (at approximately 20 km height) to 3000 km
188 (at approximately 60 km height). The ERA-5 reanalysis data was utilized for characterizing
189 the scale of the CGWs and indicated no small-scale fluctuation. According to the wavelet
190 analysis of Fig. 4d and 4e, the horizontal wavelengths of the northward propagating CGW at
191 60 km (Fig. 4a) and 40 km (Fig. 4b) were approximately 265 km and 290 km, respectively.



192

193 **Figure 4.** Temperature perturbations at (a) ~60 km , (b) ~40 km, and (c)~20 km at 23:00 LT on 4
 194 October 2016 derived from ERA-5 reanalysis. (d) Wavelet power spectrum along the red line in (a), (e)
 195 wavelet power spectrum along the red line in (b), and (f) wavelet power spectrum along the red line in
 196 (c).

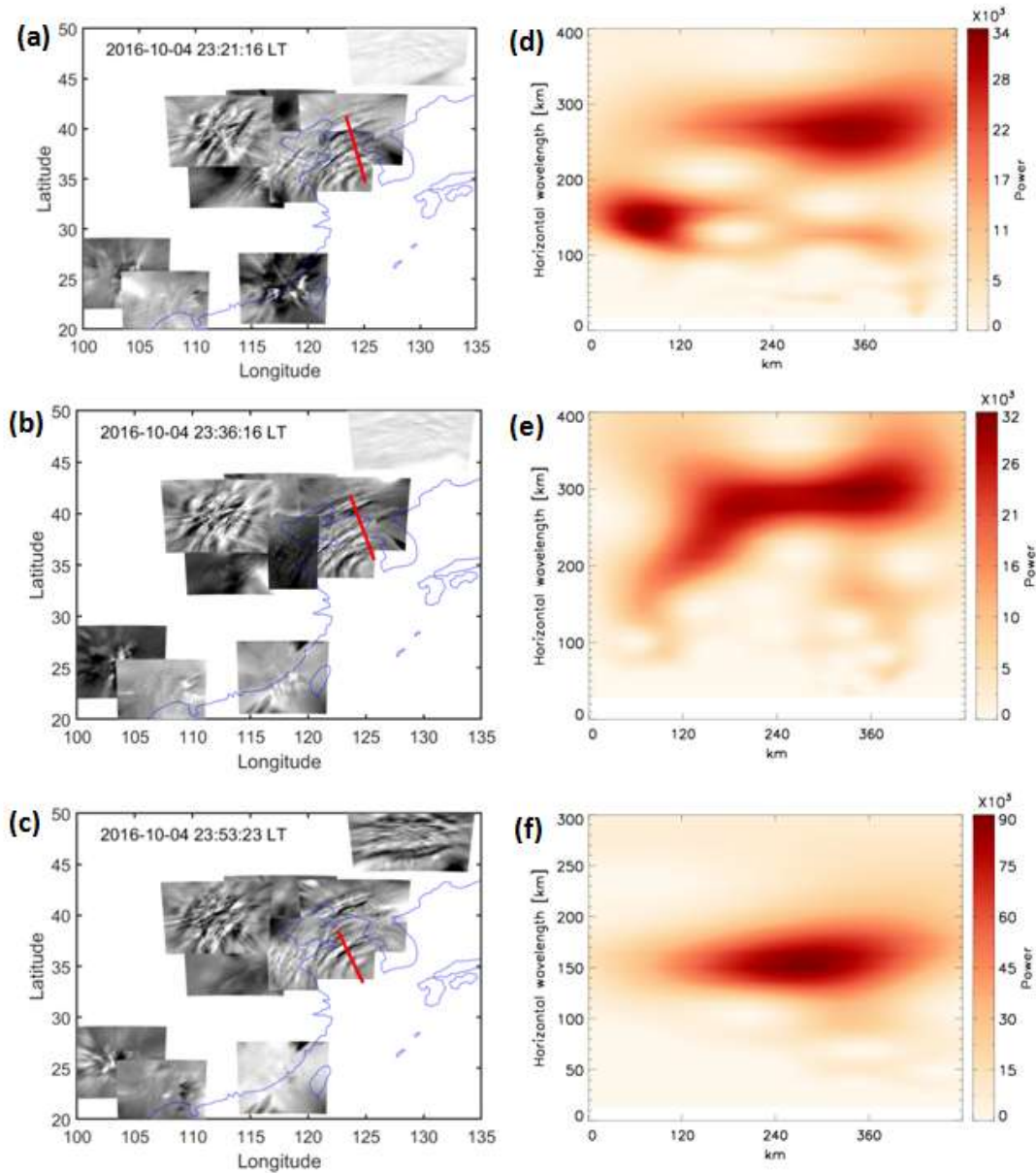
197 3.2 Propagation of typhoon-induced CGWs in the mesosphere

198 As the typhoon moved along the coast of China, CGWs were identified at ten stations
 199 in the OH network. Animation 1 shows that CGWs were observed by the OH airglow

200 network during 20:00–04:00 LT (the detailed data can be downloaded from the
201 Supplementary Material). As the weather conditions in North China during the study period
202 were better than those in South China, we identified clearer wave structures at the northern
203 stations than at the southern stations. Nevertheless, circular wave structures were visible
204 for brief clear weather intervals at the Zhangzhou, Qujing, and Chongzuo stations. The
205 CGWs in the mesopause region extended to 2500 km, thereby nearly covering the effective
206 FOV of the OH airglow network.

207 As long as the CGWs do not encounter the critical layer or break, the phase plane of
208 CGWs from ERA-5 reanalysis datasets can propagate to the OH airglow layer. Through the
209 propagation group velocity, we can determine the propagation time to the OH layer. A single
210 dominant horizontal wavelength is seen at the altitudes of 20 km, 40 km, and 60 km in the
211 ERA-5 reanalysis due to the limited resolution. In contrast, the horizontal scales of the CGW
212 obtained by the OH airglow network were diverse, ranging from approximately 30 km to
213 300 km as the imager has much higher spatial resolution. More importantly, we found some
214 CGWs in the OH airglow layer, which were close to the CGW wavelengths at 20 km, 40 km,
215 and 60 km altitudes. To verify whether the phase plane of the same wave was propagated
216 from the reanalysis data layer to the OH layer, we used the group velocity to estimate the
217 time when the phase plane of CGW at the altitudes of 20 km, 40 km, and 60 km reached the
218 OH airglow layer. The times required for the CGW in the three-layer disturbance diagram in
219 Fig. 4a, 4b, and 4c to reach the OH layer were approximately 21 minutes, 36 minutes, and
220 53 minutes. Therefore, the time when the phase plane of CGWs from ERA-5 at the height of
221 60 km, 40 km, and 20 km reaches the OH airglow layer is approximately 23:21 LT, 23:36 LT,

222 and 23:53 LT as shown in Fig. 5a, 5b, and 5c, respectively. The wavelet analysis of Fig. 5f
223 showed that the horizontal wavelength of CGW in the OH airglow layer (Fig. 5c) is
224 approximately 156 km, the observed period is approximately 23 min, and the horizontal
225 speed is approximately 113 m/s, which is similar to the dominant horizontal wavelength of
226 the CGWs in the ERA-5 reanalysis at 20 km altitude. Similarly, the horizontal wavelengths
227 of CGW in the OH airglow layers (Fig. 5a and 5b) were approximately 270 km and 295 km
228 from the wavelet analysis of Fig. 5d and 5e, which is similar to the dominant horizontal
229 wavelength of the CGWs in the ERA-5 reanalysis at 60 km and 40 km altitudes. This
230 suggests that the same CGW event can be perfectly tracked at different layer altitudes and
231 that the CGWs in the mesosphere come from the direct excitation of the typhoon.



232
 233 **Figure 5.** OH airglow emission perturbations induced by CGWs observed by the OH airglow imager
 234 network at (a) 23:21 LT, (b) 23:36 LT, and (c) 23:53 LT on 4 October 2016. (d) Wavelet power spectrum
 235 along the red line in (a), (e) wavelet power spectrum along the red line in (b), and (f) wavelet power
 236 spectrum along the red line in (c).

237 3.3 How typhoon-induced CGWs propagate to the thermosphere

238 Figure 6 shows the time sequence of the OI 630.0 nm airglow images from 00:57:05 LT
 239 to 01:12:22 LT on the night of 4 October 2016. Three curved phase fronts are clearly visible.
 240 The wave packet observed in the OI 630 nm airglow was quasi-monochromatic. According

241 to the wavelet analysis spectrum in Fig. 7, the horizontal wavelength was approximately 120
242 km. The observation period and phase velocity were 10 min and 200 m/s, respectively. The
243 horizontal wavelength was somewhat less than the multi-scale typhoon-induced concentric
244 traveling ionosphere disturbances with a horizontal wavelength from 160 to 200 km in the
245 GNSS-TEC network as reported by Chou et al. (2017). The CGW observed in the OI 630.0
246 nm airglow had much faster phase speed and shorter period, which indicate that its
247 propagation trajectory was relatively vertical. This means that they will not propagate as far
248 horizontally as the CGWs noted as dominant in the OH layer. Indeed, compared with the
249 long-distance extension of the CGWs in the mesosphere, the propagation distance of the
250 CGWs in the thermosphere was only 600 km. Numerical simulations revealed that the
251 thermosphere GWs may originate from secondary GWs generated by the breaking of primary
252 GWs in the mesosphere or thermosphere region (Vadas and Crowley, 2010). We argue that
253 the following phenomenon can represent the potential driver of this pattern. Specifically, the
254 thermospheric CGW observed by the OI 630.0 nm airglow imager was not directly
255 generated by the typhoon, but a secondary GW. To test this hypothesis, backward
256 ray-tracing analysis was applied. In this way, we determined the source of the CGW
257 observed in the thermosphere.

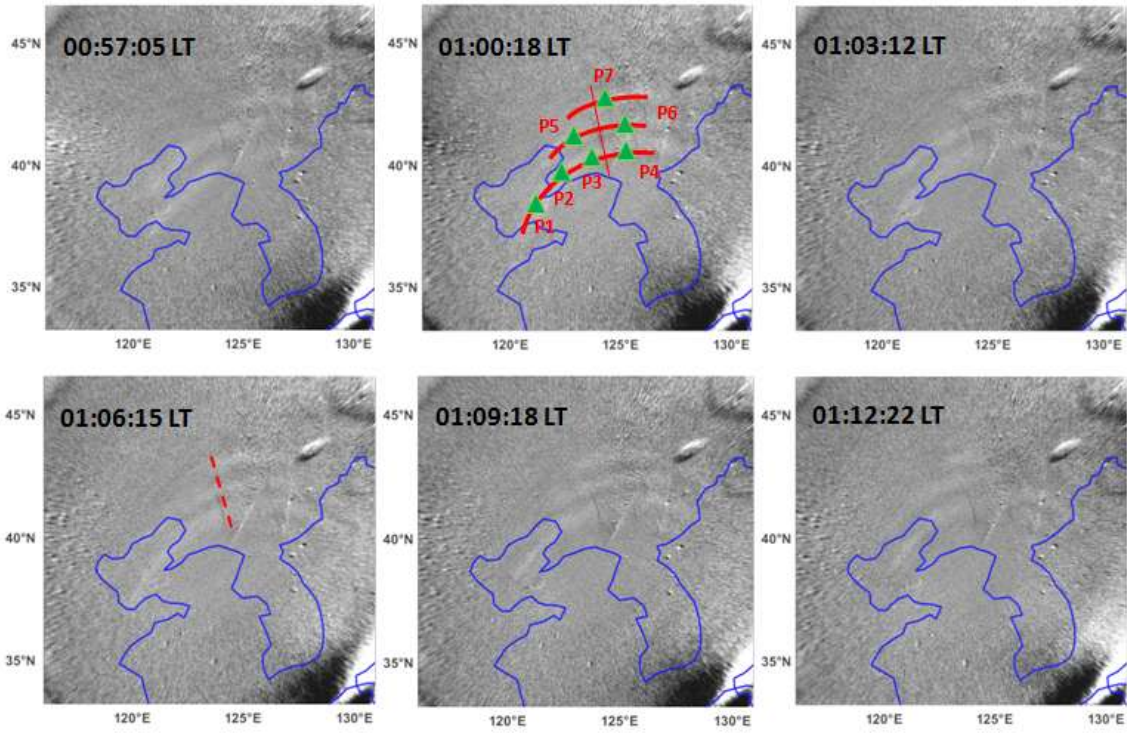


Figure 6. Time sequence of OI 630.0 nm airglow emission perturbation images observed by Donggong station during 00:57:05 – 01:12:22 LT on the night of 4 October 2016. Green triangles (P1-P7) in the red arcs are used as ray tracing sampling points. The blue line in each panel represents the coastline.

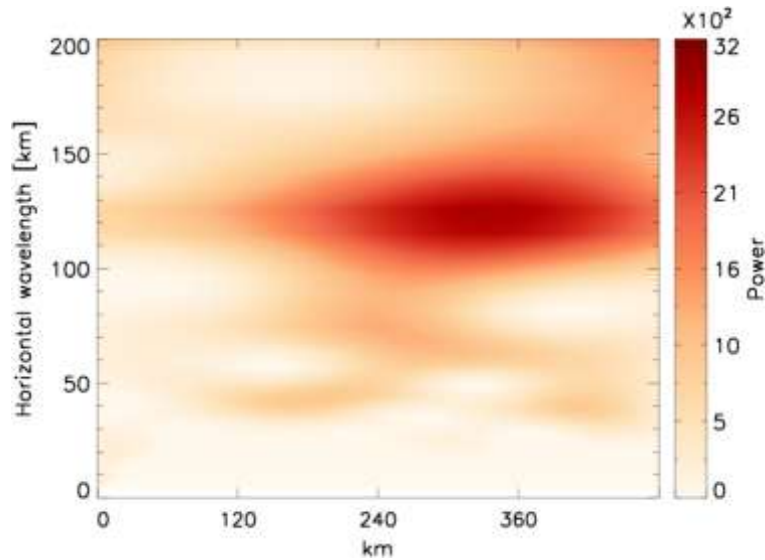
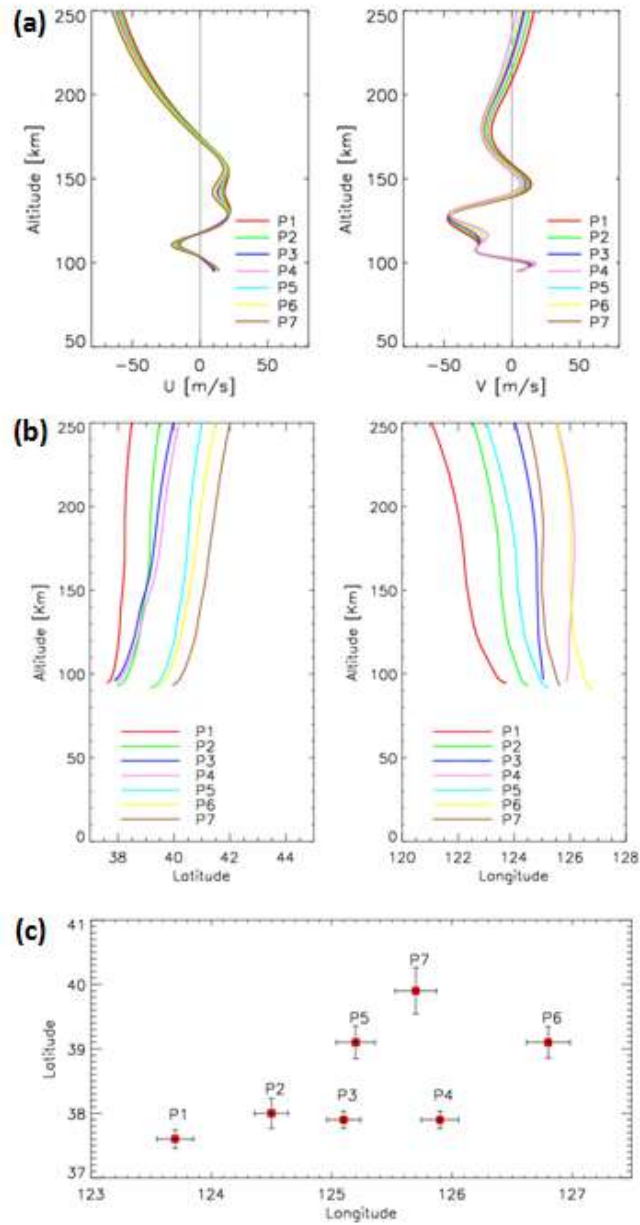


Figure 7. Wavelet power spectrum along the red line at 01:00:18 LT in Fig. 6.

We sampled seven points (green triangles) on a circular wavefront (red line in Fig. 6) at 01:00:18 LT as the starting point for backward ray tracing. The starting height of the

backward ray tracing was 250 km. The profile of the winds used in the ray tracing is shown in Fig. 8a. The ray tracing trajectories of the seven sampling points are shown in Fig. 8b. We used the following criterion to terminate the ray tracing: the square of the vertical wavenumber should be negative. The ray-tracing results of three different heights of 240 km, 250 km, and 260 km were analyzed. The maximum uncertainty of horizontal change of ray-tracing termination point caused by different starting heights was approximately $\pm 0.36^\circ$ in latitude and $\pm 0.17^\circ$ in longitude (see Figure 8c). Subsequently, seven backward traced trajectories took 37 minutes and terminated at an altitude of approximately 95 km thereby indicating that it met the reflection layer, which, according to linear theory, suggests that the thermospheric CGW could not have come from below 95 km according to linear theory. The thermospheric CGW could have been generated at any altitude between 95 km and the altitude of the OI 630.0 nm airglow. In other words, the CGW observed in the thermosphere was excited after approximately 00:23 LT. Meanwhile, Figure 9 presents the CGWs observed by the OH airglow network at 00:23:22 LT. We superimposed the thermospheric CGWs along with the starting ray tracing points (green triangles) reproduced from Fig. 6, and the backward ray tracing termination points (red diamonds) on the OH airglow observation images. The dotted circle represents the approximate fitting thermospheric CGW fronts. The center of the circle is marked by a blue cross. Compared with the single-scale wave observed in the OI 630.0 nm layer, multi-scale CGWs were visible from OH network observations. We found that the termination points of ray tracing almost fell above the mesopause region, which showing clear signs of dissipation and/or nonlinear processes. This suggests that the CGW observed in the thermosphere did not directly

originate from the typhoon but may have emerged due to the dissipation and/or nonlinear processes of typhoon-induced CGW in the mesopause region. However, the backward tracing terminal positions (red diamonds in Fig. 9) did not coincide with the fitting circle center position (blue cross in Fig. 9). Nevertheless, according to numerical simulation work by Vadas et al. (2009), large winds can shift the apparent center of concentric rings from the location of the convective plume. Indeed, we found strong southward winds from 100 km to 140 km (with a peak value of 50 m/s at 150 km altitude) and from 160 km to 220 km (with a peak value of 25 m/s at 175 km altitude) altitudes (right panel of Figure 8a). So the center of the thermospheric CGW can be shifted southward from the location of the thermospheric CGW sources in the mesopause region. For the zonal wind, the westward wind dominated from the upper mesosphere to the thermosphere (left panel of Figure 8a). Similarly, the thermospheric CGW center position shifted westward. Therefore, the assumed center (blue cross) of the partial concentric ring GWs (blue arcs) actually shifted to the southwest from the real source location, which can explain why the ray-tracing result for the assumed GW source did not match the fitting center of the partial concentric ring thermospheric GWs. As the ray-tracing model used in this study depended on the linear theory and did not consider the wave-wave and wave-mean flow interactions and tunneling, the ray tracing results were limited and should be taken into consideration carefully.



306

307 **Figure 8.** (a) Wind profiles along the seven ray-tracing paths. (b) Ray paths of the wave starting from the
 308 seven sampling points in Fig.6. (c) Horizontal area distribution of the terminal positions of the seven
 309 backward traced trajectories. Error bars give standard deviation for each point from the starting altitude of
 310 240 km, 250 km, and 260 km.

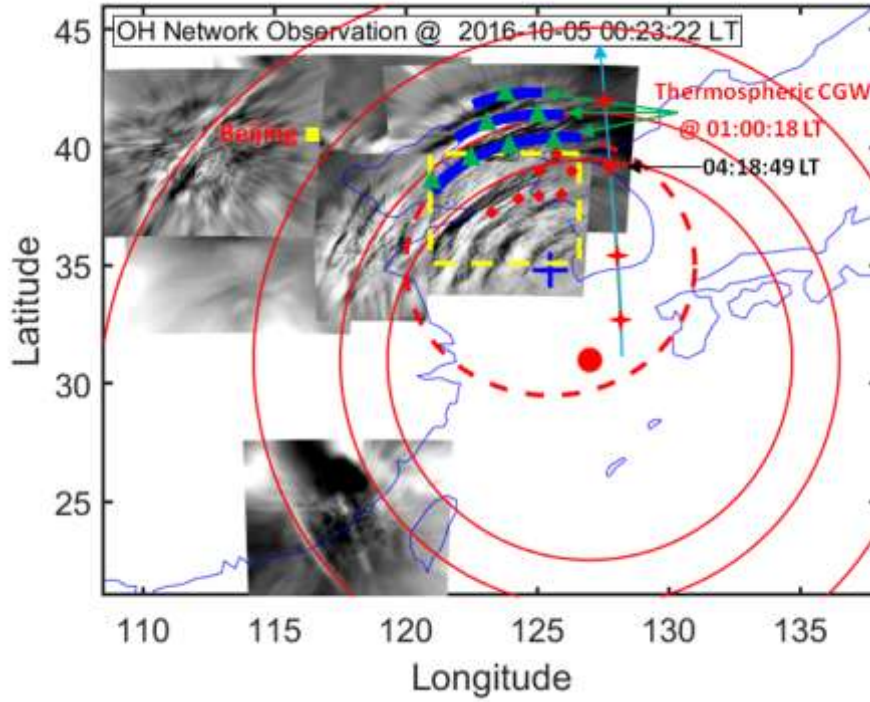


Figure 9. Double layer CGW superimposed graph: The blue arcs represent the thermospheric CGW observed at 01:00:18 LT. The dotted circle represents the approximate fitting blue arcs. The blue cross marks the center of the circle. The solid circles represent the approximate fitting CGWs observed by the OH airglow network. The red dot marks the center of the circles. The green triangles and red diamonds represent the trace start and termination points, respectively. The red crosses represent the sounding footprints of the TIMED/SABER measurements. The yellow box marks the location of the meteor radar station.

4. Discussion

Figure 10 presents a time sequence of OH airglow images in the range marked by the yellow dotted rectangle in Fig. 9. The images were retrieved from the Rongcheng station from 00:01:30 to 00:44:30 LT on the night of 4 October 2016. At 00:01:30 LT, three distinct curved wavefronts with horizontal wavelengths of approximately 96 km were identified. Interestingly, wavefronts 2 and 3 collided and connected in the northeast, indicating that wave-wave nonlinear interactions may have occurred.

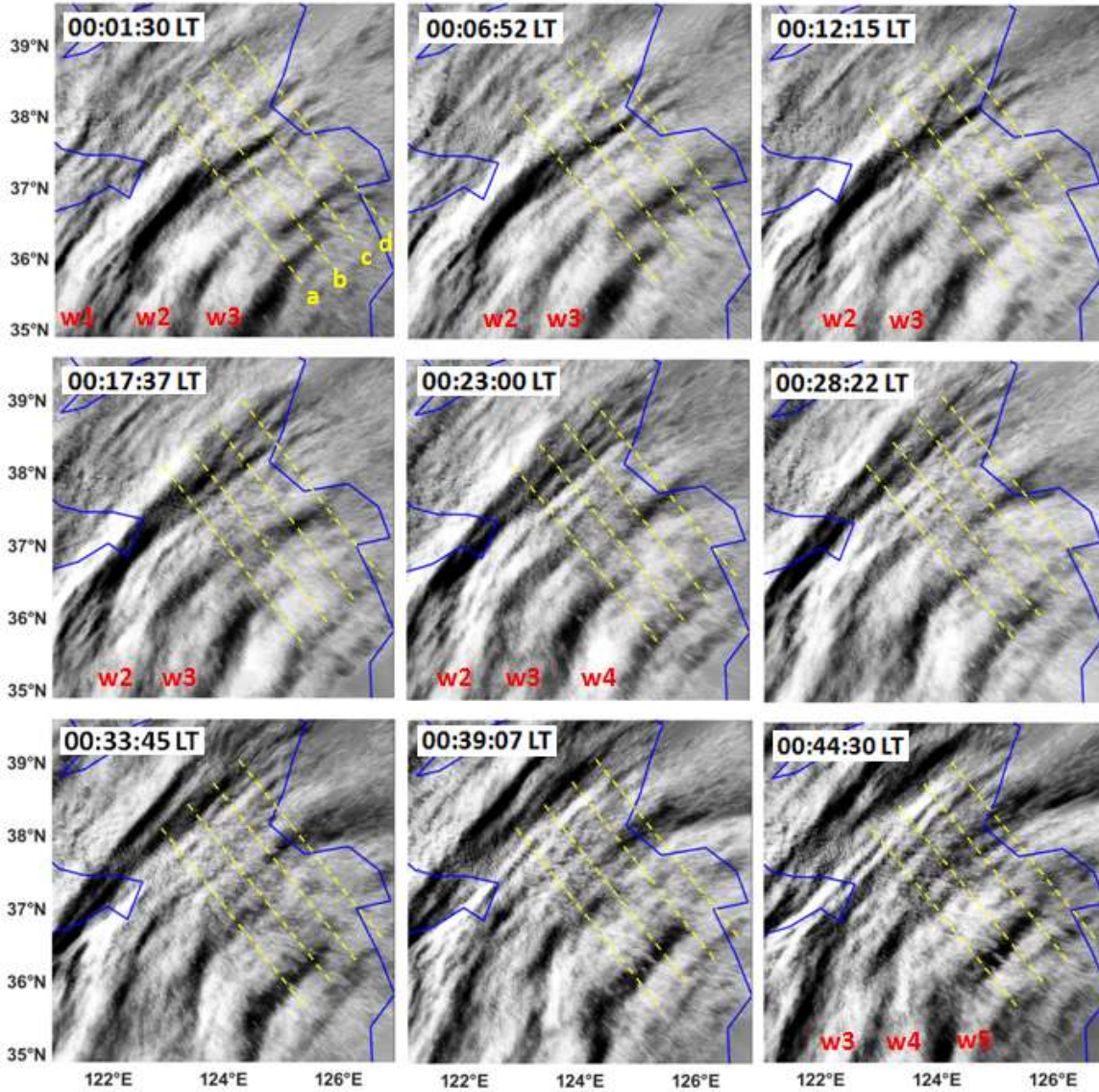
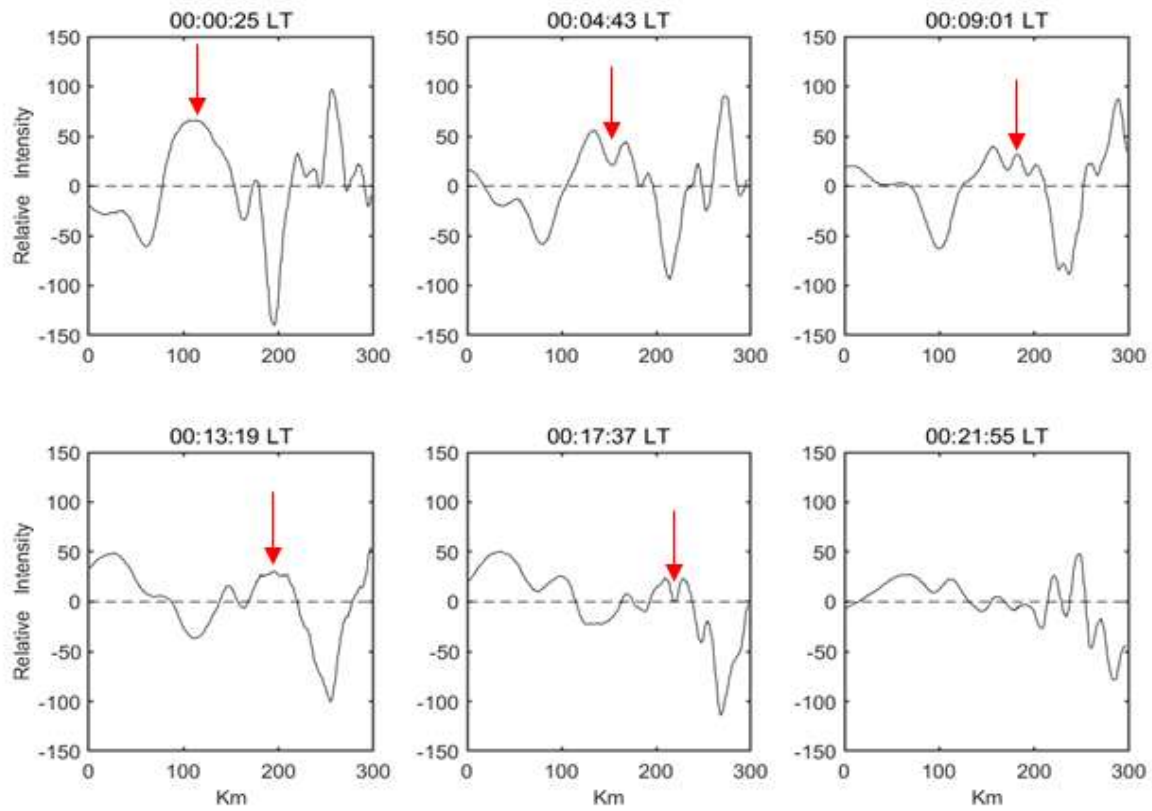


Figure 10. Time sequence of OH airglow emission perturbation images observed by Rongcheng station during 01:01:30-00:44:30 LT on the night of 4 October 2016. w1-w5 denote the wavefronts of the CGW. The blue line in each panel represents the coastline.

We elucidated the dissipation process of the CGWs in detail by examining the evolution process of their amplitude. Figure 11 shows the time series of the OH image slices perpendicular to the wavefronts. A dominant wavelength of approximately 150 km can be confirmed. As a result, we found a significant attenuation of the amplitude from 00:06:52 LT to 00:17:37 LT. At 00:06:52 LT, while the relative average power was 2.3×10^3 , and the

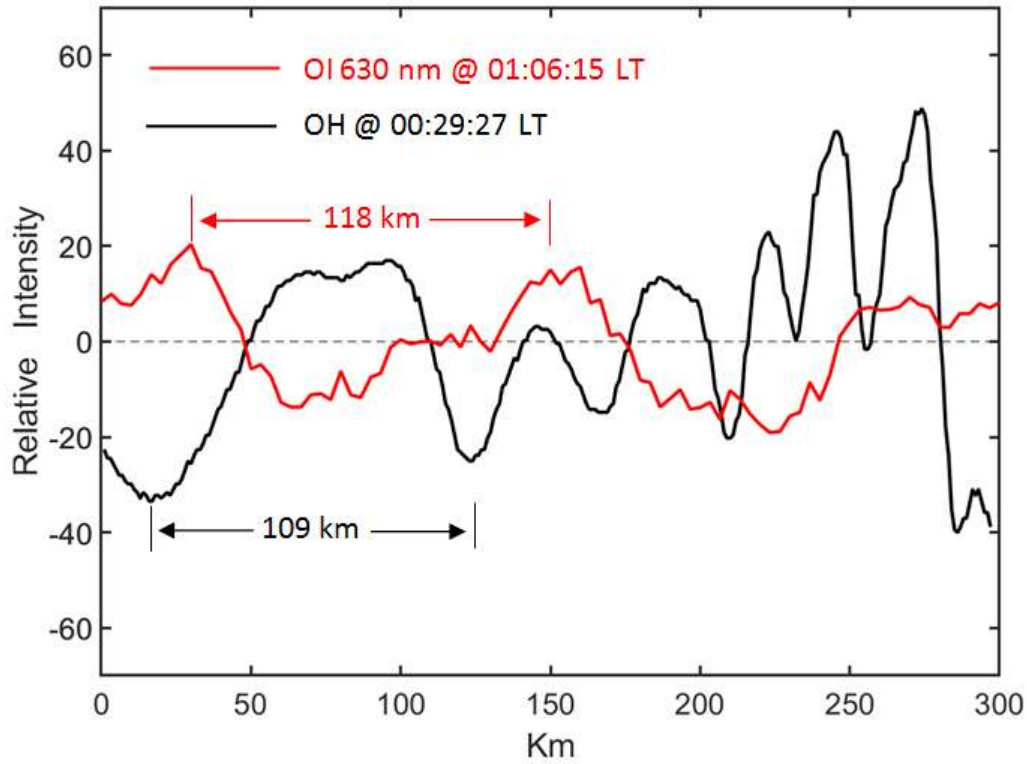
336 amplitude decreased gradually with time. At 00:17:37 LT, the average power decreased to
337 0.15×10^3 . We also identified the generation of approximately 110 km and 20-50 km
338 small-scale waves from the larger scales, which may be caused by wave-wave nonlinear
339 interactions and/or wave breaking. We overlaid the OI 630 nm airglow relative intensity
340 variation on the OH airglow variation and Figure 12 shows OH and OI 630 nm airglow
341 relative intensity variations. The OH plot was obtained at 00:29:27 LT and the OI 630 nm
342 plot at 01:06:15 LT. The time interval of 37 min was calculated by the above ray tracing
343 analysis. We obtained similar scale fluctuations were obtained in the two airglow layers. The
344 horizontal wavelength of the wave obtained by the OI 630 nm airglow layer was
345 approximately 118 km. The OH airglow layer has also obtained near-scale fluctuations with
346 wavelengths of approximately 109 km. Therefore, the CGW in the thermosphere may come
347 from breaking or nonlinear processes of that primary gravity waves.

348



349

350 **Figure 11.** Time series of averaged OH image slices perpendicular to the wavefronts as marked by four
 351 yellow dotted lines (a, b, c, and d) in Fig.10. The wavefronts propagate from left to right. The red arrows
 352 mark the evolution of the wavefront peak.



353
 354 **Figure 12.** OH (black) and OI 630 nm (red) airglow relative intensity variations. The OH relative
 355 intensity variation is obtained as in Fig. 11. The OI 630 nm relative intensity variation is from the red
 356 dotted line in Fig.10 at 01:06:15 LT.

357 However, wavepacket amplitude fluctuations can also result from the transient nature
 358 of the wavepacket. The propagation state can be studied by using the dispersion relationship
 359 with GW but the dissipation region of the CGW lacks the real-time background temperature
 360 and wind field. In this context, TIMED/SABER can be beneficial because it occurred near
 361 the wave-dissipation region; however, the time lag was close to approximately 4 h. On this
 362 basis, we used the meteor radar wind field data from the Beijing station as auxiliary
 363 information. We further examined the dispersion relationship of GW, thereby shedding some
 364 light on the possible propagation state of dissipative waves. Figure 13 presents the vertical
 365 wave number m^2 profile derived from the Beijing meteor radar wind and the temperature
 366 from the TIMED/SABER sound at 04:18:49 LT, as marked in Fig. 9. The wave parameters

367 used were from the wavefronts (w1-w5) in Fig.10. The average horizontal wavelength was
368 approximately 96 km and the average observed phase velocity is approximately 90 m/s. We
369 identified a clear duct (from 87 km to 94 km) near the peak of the OH airglow layer. Note
370 that the duct can control the horizontal propagation of CGW. This implies that the CGW
371 may indeed be dissipated. In contrast, the upper boundary of the duct coincided with the
372 height of the ray-tracing termination area mentioned above. During wave dissipation,
373 momentum deposition occurs in the background atmosphere and can produce bodyforces
374 that stimulate secondary GWs (Fritts et al., 2006; Chun and Kim, 2008; Smith et al., 2013;
375 Vadas et al., 2018; Heale et al., 2020). In addition, secondary waves can be generated by
376 momentum transferred nonlinearly from the primary wave mode to harmonics or
377 subharmonics (Snively, 2017). Local momentum flux divergence associated with wave
378 breaking, vortex generation, and wave interactions can also generate secondary GWs (Fritts
379 et al., 2006).

380

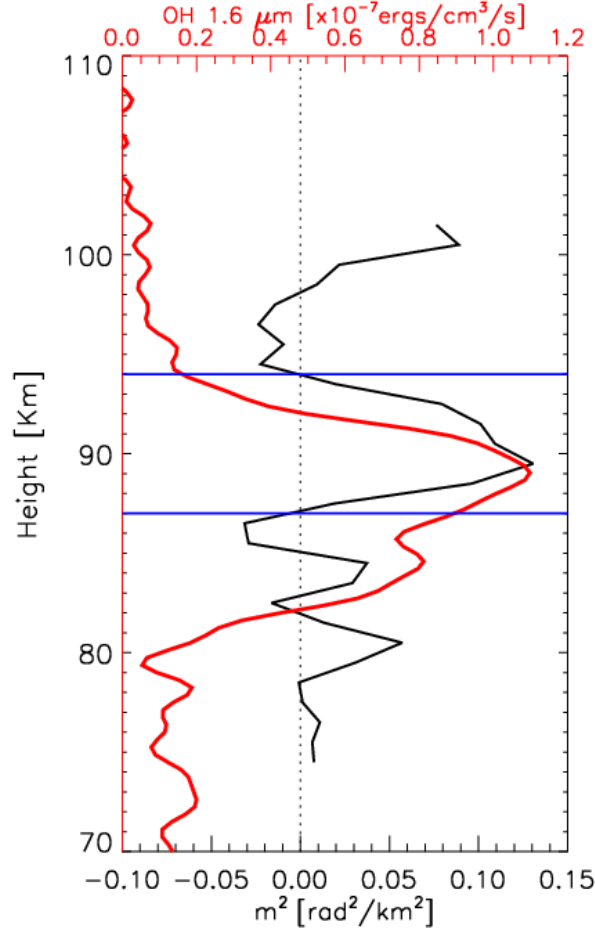


Figure 13. Vertical wave number m^2 derived from the temperature from TIMED/SABER sound at 04:18:49 LT and the meteor radar wind from Beijing station marked in Fig. 9. The red line represents the OH1.6 μm emission intensity obtained by the TIMED/SABER. The horizontal lines represent the top and bottom boundaries of the duct region.

5. Summary

In this study, a DLAN was used to capture CGWs over China that were excited by the Super Typhoon Chaba (2016). As Super Typhoon Chaba (2016) moved northward along the coast of the Chinese Mainland and developed to a mature stage, remarkable multi-layer CGW features produced by the Typhoon from near the ground to a height of 250 km were observed by ERA-5 reanalysis and airglow network. We applied the MTSAT-1R

393 observations, ERA-5 reanalysis data, and backward ray tracing to quantitatively describe the
394 physical mechanism of typhoon-generated CGWs propagating throughout the stratosphere,
395 mesosphere, and thermosphere.

396 The temperature disturbance was approximately $\pm 1.5\text{-}2$ K at 20 km and $\pm 3\text{-}4$ K at 40
397 km. However, the temperature disturbance (± 1.3 K) at 60 km altitude did not increase with
398 further increase in altitude, which may be caused by the sponge layer effect. Using
399 reanalysis of multi-layer temperature disturbance, group velocity of gravity wave and
400 wavelet analysis, we demonstrated that the CGWs in the mesopause region were excited
401 directly by the typhoon.

402 Due to the observational limitations, a backward ray-tracing theory was used to connect
403 the upper mesosphere and GWs to the thermosphere. We found that the termination points of
404 ray tracing of the thermospheric CGW almost fell above the mesopause region, which shows
405 clear signs of primary CGW dissipation and/or nonlinear processes. Backward ray-tracing
406 analysis and the CGWs evolution process observed by OH network suggested that the CGW
407 observed in the thermosphere did not directly originate from the typhoon but may have
408 emerged due to dissipation and/or nonlinear processes of typhoon-induced CGWs in the
409 mesopause region. Airglow network observations combined with numerical simulation to
410 study the generation of secondary wave in detail will be carried out in the future.

411

412 ***Data availability***

413 The Double Layer Airglow Network data are available at <http://159.226.22.74/>. The ERA-5
414 reanalysis data are downloaded from the Copernicus Climate Change Service Climate Data

415 Store through <https://www.ecmwf.int/en/forecasts/datasets/reanalysis-datasets/era5>. The
416 typhoon information are provided at <http://agora.ex.nii.ac.jp/digital-typhoon/>. MTSAT-1R
417 data is accessed from <http://webgms.iis.u-tokyo.ac.jp/>.

418

419 ***Video supplement***

420 A video of detailed evolutions of CGWs excited by the Typhoon observed by OH airglow
421 observation network is provided (<https://doi.org/10.5446/55348>).

422

423 ***Author contributions***

424 J. X conceived the idea of the manuscript. Q. L. carried out the data analysis, interpretation
425 and manuscript preparation. H. L. L., X. L and W. Y. contributed to the data interpretation
426 and manuscript preparation. All authors discussed the results and commented on the
427 manuscript.

428

429 ***Competing interests***

430 The authors declare no competing interests.

431

432 ***Acknowledgements***

433 This work was supported by the National Science Foundation of China (41974179 and
434 41831073), Pandeng Program of National Space Science Center, Chinese Academy of
435 Sciences and the Strategic Priority Research Program of Chinese Academy of Sciences
436 (XDA17010301), and the Informatization Plan of Chinese Academy of Sciences

437 (CAS-WX2021PY-0101). The work was also supported by the Specialized Research Fund
438 for State Key Laboratories. We acknowledge the use of data from the Chinese Meridian
439 Project.

440

441 **References**

442 Azeem, I., Yue, J., Hoffmann, L., Miller, S. D., Straka, W. C., and Crowley, G.: Multisensor
443 profiling of a concentric gravity wave event propagating from the troposphere to the
444 ionosphere, *Geophys. Res. Lett.*, 42, 7874–7880, 2015.

445 Becker, E., Vadas, S. L., Bossert, K., Harvey, V. L., Zülicke, C., and Hoffmann, L.: A
446 High-resolution whole atmosphere model with resolved gravity waves and specified
447 large-scale dynamics in the troposphere and stratosphere, *Journal of Geophysical*
448 *Research: Atmospheres*, 127, 2022.

449 Chun, H.-Y., and Kim, Y.-H.: Secondary waves generated by breaking of convective gravity
450 waves in the mesosphere and their influence in the wave momentum flux, *J. Geophys.*
451 *Res.*, 113, D23107, 2008.

452 Chou, M. Y., Lin, C. C. H., Yue, J., Tsai, H. F., Sun, Y. Y., Liu, J. Y., and Chen, C. H.:
453 Concentric traveling ionosphere disturbances triggered by Super Typhoon Meranti
454 (2016), *Geophys. Res. Lett.*, 44, 1219–1226, 2017.

455 Dong, W., Fritts, D. C., Lund, T. S., Wieland, S. A., and Zhang, S.: Self - acceleration and
456 instability of gravity wave packets: 2. two - dimensional packet propagation, instability
457 dynamics, and transient flow responses, *Journal of Geophysical Research: Atmospheres*,
458 125, 2020.

459 Drob, D. P., Emmert, J. T., Meriwether, J. W., Makela, J. J., Doornbos, E., Conde, M., et al. An
 460 update to the Horizontal Wind Model(HWM): The quiet time thermosphere, *Earth and*
 461 *Space Science*, 2, 301–319, 2015.

462 Duncombe, J.: The surprising reach of Tonga’s giant atmospheric waves, *Eos*, 103,
 463 <https://doi.org/10.1029/2022EO220050>, 2022.

464 Franke, P. M. and Robinson, W. A.: Nonlinear behavior in the propagation of atmospheric
 465 gravity waves, *J. Atmos. Sci.*, 56, 3010-3027, 1999.

466 Fritts, D. C. and Alexander, M. J.: Gravity wave dynamics and effects in the middle
 467 atmosphere, *Rev. Geophys.*, 41(1), 1003, 2003.

468 Fritts, D. C., Vadas, S. L., Wan, K., and Werne J. A.: Mean and variable forcing of the middle
 469 atmosphere by gravity waves, *J. Atmos. Sol. Terr. Phys.*, 68, 247–265, 2006.

470 Fritts, D. C., B. Laughman, T. S. Lund, and Snively, J. B.: Self-acceleration and instability of
 471 gravity wave packets:1. Effects of temporal localization, *J. Geophys. Res. Atmos.*, 120,
 472 8783–8803, 2015.

473 Fritts, D. C., Dong, W., Lund, T. S., Wieland, S., and Laughman, B.: Self - acceleration and
 474 instability of gravity wave packets: 3.Three - dimensional packet propagation,
 475 secondary gravity waves, momentum transport, and transient mean forcing in tidal winds,
 476 *Journal of Geophysical Research: Atmospheres*, 125, 2020.

477 Garcia, F. J., Taylor, M. J., and Kelly, M. C.: Two - dimensional spectral analysis of
 478 mesospheric airglow image data, *Applied Optics*, 36(29), 7374–7385,1997.

479 Gavrilov, N. M. and Kshevetskii, S. P.: Features of the Supersonic Gravity Wave Penetration
 480 from the Earth's Surface to the Upper Atmosphere, *Radio physics and Quantum*
 481 *Electronics*, 61(4), 243-252, 2018.

482 Heale, C. J., Snively, J. B., Bhatt, A. N., Hoffmann, L., Stephan, C. C., and Kendall, E. A.:
 483 Multilayer observations and modeling of thunderstorm-generated gravity waves over the
 484 Midwestern United States. *Geophysical Research Letters*, 46, 14,164–14,174.
 485 <https://doi.org/10.1029/2019GL085934>, 2019.

486 Heale, C. J., Bossert, K., Vadas, S. L., Hoffmann, L., Dornbrack, A., Stober, G., et al.
 487 Secondary gravity waves generated by breaking mountain waves over Europe, *Journal*
 488 *of Geophysical Research: Atmospheres*, 125, e2019JD031662, 2020.

489 Heale, C. J., Inchin, P. A., and Snively, J. B.: Primary Versus Secondary Gravity Wave
 490 Responses at F-Region Heights Generated by a Convective Source, *Journal of*
 491 *Geophysical Research: Space Physics*, <https://doi.org/10.1029/2021JA029947>, 2021.

492 Hersbach, H., Bell, B., Berrisford, P., Hirahara, S., Horányi, A., Muñoz-Sabater, J., Nicolas, J.,
 493 Peubey, C., Radu, R., Schepers, D., Simmons, A., Soci, C., Abdalla, S., Abellan, X.,
 494 Balsamo, G., Bechtold, P., Biavati, G., Bidlot, J., Bonavita, M., De Chiara, G., Dahlgren,
 495 P., Dee, D., Diamantakis, M., Dragani, R., Flemming, J., Forbes, R., Fuentes, M., Geer,
 496 A., Haimberger, L., Healy, S., Hogan, R. J., Hólm, E., Janisková, M., Keeley, S.,
 497 Laloyaux, P., Lopez, P., Lupu, C., Radnoti, G., de Rosnay, P., Rozum, I., Vamborg, F.,
 498 Villaume, S., and Thépaut, J. N.: The ERA5 global reanalysis, *Q. J. R. Meteorol. Soc.*,
 499 146(730), 1999–2049, doi:10.1002/qj.3803, 2020.

500 Hoffmann, L., Günther, G., Li, D., Stein, O., Wu, X., Griessbach, S., Heng, Y., Konopka, P.,

501 Müller, R., Vogel, B. and Wright, J. S.: From ERA-Interim to ERA5: The considerable
 502 impact of ECMWF's next-generation reanalysis on Lagrangian transport simulations,
 503 Atmos. Chem. Phys., 19(5), 3097–3214, doi:10.5194/acp-19-3097-2019, 2019.

504 Holton, J.R.: The influence of gravity wave breaking on the general circulation of the middle
 505 atmosphere, J. Atmos. Sci., 40, 2497–2507, 1983.

506 Kogure, M., Yue, J., Nakamura, T., Hoffmann, L., Vadas, S. L., Tomikawa, Y., Ejiri, M. K.,
 507 and Janches, D.: First direct observational evidence for secondary gravity waves
 508 generated by mountain waves over the Andes. Geophysical Research Letters, 47, 2020.

509 Kim, S.-Y., Chun, H.-Y., and Wu, D. L.: A study on stratospheric gravity waves generated by
 510 Typhoon Ewiniar: Numerical simulations and satellite observations, J. Geophys. Res.,
 511 114, D22104, 2009.

512 Li, Q., Xu, J., Yue, J., Yuan, W., and Liu, X.: Statistical characteristics of gravity wave
 513 activities observed by an OH airglow imager at Xinglong, in northern China, Annales
 514 Geophysicae, 29 (8), 1401–1410, 2011.

515 Liu, H.-L. and Vadas, S. L.: Large-scale ionospheric disturbances due to the dissipation of
 516 convectively-generated gravity waves over Brazil, J. Geophys. Res. Sp. Phys., 118(5),
 517 2419–2427, doi:10.1002/jgra.50244, 2013.

518 Liu, H.-L., McInerney, J. M., Santos, S., Lauritzen, P. H., Taylor, M. A., and Pedatella, N.
 519 M.: Gravity waves simulated by high-resolution Whole Atmosphere Community
 520 Climate Model, Geophys. Res. Lett., 41, 9106–9112, 2014.

521 Liu, H., Ding, F., Yue, X., Zhao, B., Song, Q., Wan, W., Ning, B., Zhang, K.: Depletion and

522 traveling ionospheric disturbances generated by two launches of China's Long March 4B
523 rocket. *Journal of Geophysical Research: Space Physics*, 123, 10,319–10,330, 2018.

524 Lund, T. S. and Fritts, D. C.: Numerical simulation of gravity wave breaking in the lower
525 thermosphere, *J. Geophys. Res. Atmos.*, 117, D21105, 10.1029/2012jd017536, 2012.

526 Lund, T. S., Fritts, D. C., Wan, K., Laughman, B., and Liu, H.-L.: Numerical Simulation of
527 Mountain Waves over the Southern Andes. Part I: Mountain Wave and Secondary Wave
528 Character, Evolutions, and Breaking, *Journal of the Atmospheric Sciences*, 77(12),
529 4337-4356, 2020.

530 Pfeffer, R. L. and Zarichny, J.: Acoustic-Gravity Wave Propagation from Nuclear
531 Explosions in the Earth's Atmosphere, *J. Atmos. Sci.* 19, 256–263, 1962.

532 Picone, J. M., Hedin, A. E., Drob, D. P., and Aikin, A. C. NRLMSISE - 00 empirical model of
533 the atmosphere: Statistical comparisons and scientific issues, *Journal of Geophysical*
534 *Research*, 107(A12), 1468, 2002.

535 Pierce, A.D., J. W. Posey, and Iliff, E. F.: Variation of nuclear explosion generated
536 acoustic-gravity wave forms with burst height and with energy yield, *J. Geophys. Res.*,
537 76, 5025-5042, 1971.

538 Sentman, D. D., Wescott, E. M., Picard, R. H., Winick, J. R., Stenbaek-Nielsen, H. C.,
539 Dewan, E. M., Moudry, D. R., Sao Sabbas, F. T., Heavner, M. J., and Morrill, J.:
540 Simultaneous observations of mesospheric gravity waves and sprites generated by a
541 midwestern thunderstorm, *J. Atmos. Sol. Terr. Phys.*, 65, 537–550, 2003.

542 Smith, S. M., Vadas, S. L., Baggaley, W. J., Hernandez, G., and Baumgardner, J.: Gravity
543 wave coupling between the mesosphere and thermosphere over New Zealand, *Journal of*
544 *Geophysical Research: SpacePhysics*, 118, 2694–2707, 2013.

545 Smith, S. M., Setvák, M., Beletsky, Y., Baumgardner, J., and Mendillo, M.: Mesospheric
546 gravity wave momentum flux associated with a large thunderstorm complex, *Journal of*
547 *Geophysical Research: Atmospheres*, 125, e2020JD033381, 2020.

548 Snively, J. B.: Nonlinear gravity wave forcing as a source of acoustic waves in the
549 mesosphere, thermosphere, and ionosphere, *Geophysical Research Letters*, 44,
550 12,020–12,027, 2017.

551 Suzuki, S., Shiokawa, K., Otsuka, Y., Ogawa, T., Nakamura, K., and Nakamura, T.: A
552 concentric gravity wave structure in the mesospheric airglow images, *J. Geophys.*
553 *Res.*, 112, D02102, 2007.

554 Suzuki, S., Vadas, S. L., Shiokawa, K., Otsuka, Y., Kawamura, S., and Murayama, Y.:
555 Typhoon-induced concentric airglow structures in the mesopause region, *Geophys. Res.*
556 *Lett.*, 40, 5983–5987, 2013.

557 Taylor, M. J. and Hapgood, M. A.: Identification of a thunderstorm as a source of short period
558 gravity waves in the upper atmospheric nightglow emissions, *Planet. Space Sci.*, 36,
559 975–985, 1988.

560 Vadas, S. L., Fritts, D. C., and Alexander, M. J.: Mechanism for the generation of secondary
561 waves in wave breaking regions, *Journal of the Atmospheric Sciences*, 60, 194–214,
562 2003.

563 Vadas, S. L. and Fritts, D. C.: Thermospheric responses to gravity waves: Influences of
 564 increasing viscosity and thermal diffusivity, *J. Geophys. Res.*, 110, D15103,
 565 doi:10.1029/2004JD005574, 2005

566 Vadas, S. L.: Horizontal and vertical propagation and dissipation of gravity waves in the
 567 thermosphere from lower atmospheric and thermospheric sources, *Journal of*
 568 *Geophysical Research*, 112, A06305, 2007.

569 Vadas, S. L., Yue, J., She, C. Y., Stamus, P., and Liu, A. Z.: A model study of the effects
 570 of winds on concentric rings of gravity waves from a convective plume near Fort
 571 Collins on 11 May 2004, *J. Geophys. Res.*, 114, 2009.

572 Vadas, S. L. and Crowley, G.: Sources of the traveling ionospheric disturbances observed by
 573 the ionospheric TIDDBIT sounder near Wallops Island on 30 October 2007, *Journal of*
 574 *Geophysical Research*, 115, A07324, 2010.

575 Vadas, S., Yue, J., and Nakamura, T.: Mesospheric concentric gravity waves generated by
 576 multiple convective storms over the North American Great Plain, *J. Geophys. Res.*, 117,
 577 2012.

578 Vadas, S. L. and Liu, H.-L.: Numerical modeling of the large-scale neutral and plasma
 579 responses to the body forces created by the dissipation of gravity waves from 6 h of deep
 580 convection in Brazil, *J. Geophys. Res. Sp. Phys.*, 118(5), 2593–2617,
 581 doi:10.1002/jgra.50249, 2013.

582 Vadas, S. L., Zhao, J., Chu, X., and Becker, E. The excitation of secondary gravity waves
 583 from local body forces: Theory and observation, *Journal of Geophysical Research*:

584 Atmospheres, 123, 9296–9325, 2018.

585 Vadas, S. L. and Becker, E.: Numerical modeling of the generation of tertiary gravity waves in
586 the mesosphere and thermosphere during strong mountain wave events over the Southern
587 Andes. *Journal of Geophysical Research: Space Physics*, 124, 7687–7718.
588 <https://doi.org/10.1029/2019JA026694>, 2019.

589 Vadas, S. L. and Azeem, I.: Concentric Secondary Gravity Waves in the Thermosphere and
590 Ionosphere over the Continental United States on 25 - 26 March 2015 from Deep
591 Convection, *Journal of Geophysical Research: Space Physics*, 126, e2020JA028275,
592 2021.

593 Walterscheid, R. L. and Hecht, J. H.: A reexamination of evanescent acoustic-gravity waves:
594 Special properties and aeronomical significance, *J. Geophys. Res.*, 108(D11), 4340,
595 doi:10.1029/2002JD002421, 2003.

596 Xu, J., Li, Q., Yue, J., Hoffmann, L., Straka, W. C., Wang, C., Liu, M., Yuan, W., Han, S.,
597 Miller, S.D., Sun, L., Liu, X., Liu, W., Yang, J., and Ning, B.: Concentric gravity waves
598 over northern China observed by an airglow imager network and satellites, *J. Geophys.*
599 *Res. Atmos.*, 120, 11,058–11,078, 2015.

600 Xu, J., Li, Q., Sun, L., Liu, X., Yuan, W., Wang, W., Yue, J., Zhang, S., Liu, W., Jiang, G., Wu,
601 K., Gao, H., and Lai, C.: The Ground - Based Airglow Imager Network in China:
602 Recent Observational Results, *Geophysical Monograph Series*, 261, 365-394, 2021.

603 Xu, S., Yue, J., Xue, X., Vadas, S. L., Miller, S. D., Azeem, I., et al. Dynamical coupling
604 between Hurricane Matthew and the middle to upper atmosphere via gravity waves,

605 Journal of Geophysical Research: Space Physics, 124,3589–3608, 2019.

606 Yue, J., Vadas, S. L., She, C. Y., Nakamura, T., Reising, S. C., Liu, H. L., Stamus, P., Krueger,
607 D. A., Lyons, W., and Li, T.: Concentric gravity waves in the mesosphere generated by
608 deep convective plumes in the lower atmosphere near Fort Collins, Colorado, J. Geophys.
609 Res. Atmos., 114(6), 1–12, doi:10.1029/2008JD011244, 2009.

610 Yue, J., Miller, S. D., Hoffmann, L., and Straka, W. C.: Stratospheric and mesospheric
611 concentric gravity waves over tropical cyclone Mahasen: Joint AIRS and VIIRS satellite
612 observations, Journal of Atmospheric and Solar - Terrestrial Physics, 119, 83–90, 2014.

613 Zhou, X., Holton, J. R., and Mullendore, G. L.: Forcing of secondary waves by breaking of
614 gravity waves in the mesosphere, J. Geophys. Res. Atmos., 107, 2002.